Electric supplementary information:

Ionic liquid-assisted synthesis of ordered porous polymers and carbon materials: the self-assembly mechanism

Yaoguang Song,[a] Fraser Norris,[b] Daryl Hinchcliffe,[a] Yong Xu,[c] Xiaolei Zhang,[*b] and Peter Nockemann[*a]

[a]The QUILL Research Centre, School of Chemistry and Chemical Engineering, Queen's University Belfast, BT9 5AG, Belfast, UK. Email: p.nockemann@qub.ac.uk
[b]Department of Chemical and Process Engineering, University of Strathclyde, G1 1XJ, Glasgow, UK. Email: xiaolei.zhang@strath.ac.uk
[c]Jiangsu Co-Innovation Center of Efficient Processing and Utilization of Forest Resources, College of Chemical Engineering, Nanjing Forestry University, Nanjing 210037, People's Republic of China

Methodology

Multi-scale modelling, from the most accurate quantum mechanics (QM) to molecular dynamics (MD) simulations, has been regarded as a powerful assistant tool to gain insight at an atomistic/molecular level. Therefore, to study the self-assembly behaviour of ionic liquids (ILs), various empirical models have been developed including atomistic[1–3] and coarse-grained (CG) models[4,56–151617]. However, atomistic models are limited within the study of structural/dynamic properties or initial micellization of ILs.[18–21] CG models that trade explicit atomistic interactions for computational speed, are more fittingly poised to probe the mesoscopic organisation or self-assembly behaviour considering the intrinsic slow nature of these spontaneous processes.[20]

In this work, CGMD simulations were only employed to study the self-assembly behaviour of ternary mixtures containing IL templates, polymer precursor, and solvent. Detailed interactions were investigated by performing density functional theory (DFT) calculations. Experimental techniques were also carried out wherever possible to provide solid *in situ* evidence.

1. CG-MD simulations

Compatible CG models for cation and anion were based on MARTINI version 2.2 force field[22], and derived from the works of Crespo *et al.*[17] and Huet *et al.*[23] respectively. As shown in Figure S1, the IL cation is comprised of 6 beads, labelled cation n (n=1-6), where beads cation 1-3 represent imidazolium ring and cation 4-6 the alkyl chain. The carbon atoms on the alkyl chain of cation are labelled C1-C10 (from the first carbon atom attached to the imidazolium ring to the terminal carbon atom). All phenolic compounds were coarse-grained into three beads to maintain the planarity of aromatic rings; their models were based on benzene model[24] and chlorobenzene model[25]. Beads containing hydroxyl groups were represent by SP1 particles while the rest by SC5 particles. Bond length of SC5-SP1 and SP1-SP1 were refined into 0.30 and 0.31 nm, slightly larger than original value of 0.27 nm for SC5-SC5 in benzene model to match the alterations of both geometric centre and mass centre in phenolic compounds.
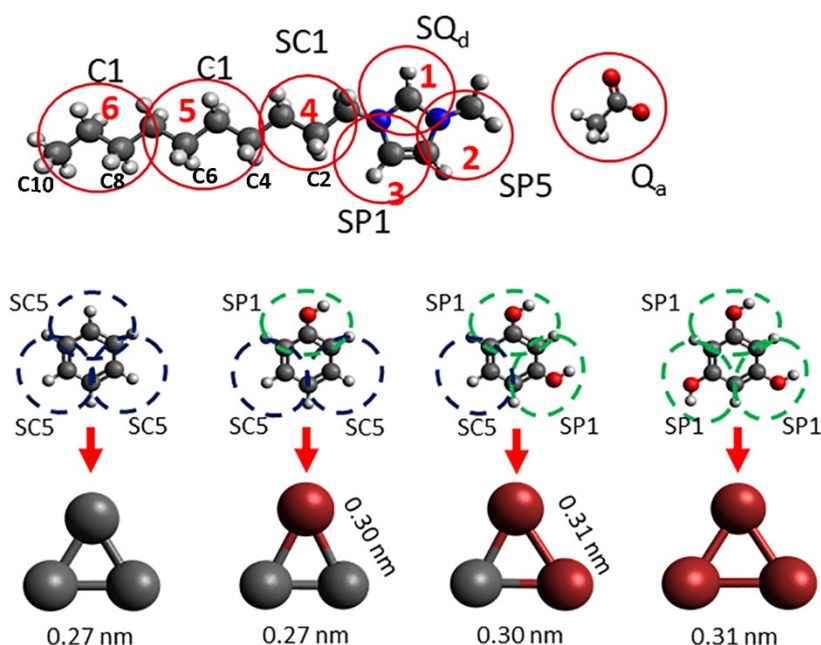

Figure S1 CG models employed in this work

The IL content in the aqueous solutions ranged from 10 wt% to 82 wt%, while the polymer precursors, phenolic compounds, were added individually at constant molar ratio of IL:phenolic compound 1:1. Initial configurations of the three-component systems were built randomly by PACKMOL[26] to ensure all the simulations started from a heterogeneous state. Non-bonded interactions were described by a shifted Lennard-Jones 12-6 and Coulomb potentials with a cut-off of 11 Å. Long-range Coulombic interactions were calculated by particle-particle particle-mesh (pppm) method with a tolerance of 10^{-5}. Energy minimisation was first performed using conjugate gradient algorithm with a stopping tolerance of 10^{-8} and 10^{-10} for energy and force respectively, followed by a simulation in NPT ensemble at 358.15 K then quenched to 298.15 K to reach equilibrium. The reason to start from higher temperature is to provide a higher kinetic energy to avoid systems from being trapped in local energy minimum rather than overall minimum. Pressure and temperature were constrained at 1 atm by the Martyna-Tobias-Klein (MTK) barostat[27], and Nose-Hoover thermostat[28,29]. All CGMD simulations were performed on LAMMPS[30] and trajectory files from the simulation were visualised on VMD package[31]. The timestep for simulation was 10 fs and production runs were recorded for 2 µs. Table S1 summarises all the simulations.

Table S1 Summary of ternary systems with final morphologies from CGMD simulations

Mixtures	$\frac{water}{IL+water} wt\%$	Precursor	Morphologies from simulation	
ILs + water + phenolics			298.15 K	358.15 K
1000 + 140000 + 1000	89.9 wt%	phenol	spherical	spherical
2000 + 125400 + 2000	80.0 wt%	phenol	spherical	spherical
3000 + 72000 + 3000	60.5 wt%	phenol	spherical	spherical
3000 + 48000 + 3000	50.5 wt%	phenol	spherical	spherical
3250 + 40000 + 3250	44.0 wt%	phenol	hexagonal columnar	spherical
3500 + 36000 + 3500	39.6 wt%	phenol	hexagonal columnar	hexagonal columnar
4000 + 32000 + 4000	33.8 wt%	phenol	hexagonal columnar	hexagonal columnar
4300 + 28000 + 4300	29.3 wt%	phenol	hexagonal columnar	lamellar bilayer
4600 + 24000 + 4600	25.0 wt%	phenol	lamellar bilayer	lamellar bilayer
4600 + 16000 + 4600	18.2 wt%	phenol	lamellar bilayer	lamellar bilayer
3250 + 40000 + 3250	44.0 wt%	resorcinol	spherical	spherical
4000 + 32000 + 4000	33.8 wt%	resorcinol	spherical	spherical
4600 + 24000 + 4600	25.0 wt%	resorcinol	hexagonal columnar	hexagonal columnar
4600 + 16000 + 4600	18.2 wt%	resorcinol	hexagonal columnar	hexagonal columnar
4600 + 24000 + 4600	25.0 wt%	phloroglucinol	spherical/rod-like	spherical/rod-like
4600 + 16000 + 4600	18.2 wt%	phloroglucinol	hexagonal columnar	hexagonal columnar
4600 + 16000 + 4600	18.2 wt%	benzene	lamellar bilayer	lamellar bilayer
4600 + 16000 + 0	18.2 wt%	n/a	hexagonal columnar	hexagonal columnar

2. DFT calculations

DFT calculations were carried out with Gaussian 16 program[32]. M06-2X method was employed at the def2-TZVP level with an additional D3 dispersion correction. No symmetry constraints were imposed during the calculations. Natural bond orbital (NBO) analysis was performed to study the H-bonding interactions within all ternary systems, atomic charges, and the stabilization energy of the electron delocalization ($E^{(2)}_{n\rightarrow\sigma*}$). In comparison with NBO analysis, quantum theory of atoms in molecules (QTAIM) analysis was also performed with Multiwfn program[33] to analyse the H-bonding interactions by finding values at the bond critical point (BCP), namely the electron density at the BCP (ρ_{BCP}), the Laplacian of the electron density at the BCP ($\nabla^2\rho_{BCP}$), and electron energy density at the BCP (H_{BCP}). The ρ_{BCP} values were used to estimate H-bond energies in kJ/mol using the correlation for a charged ionic liquid system proposed by Emamian and coworkers[34].

$$E_{H-bond} = -1390.5 \times \rho_{BCP}/a.\,u. -4.4606$$

3. Experiments

1) Synthesis of 1-decyl-3-methylimidazolium acetate

[C₁₀MIM][OAc] was prepared through a typical two-step method: the alkylation of 1-methylimidazole with 1-bromodecane and a metathesis reaction for anion exchange from a bromide to acetate.

In a typical procedure, 1-methylimidazole (0.40 mol, 99%, Sigma-Aldrich) was mixed in toluene (400 mL, ≥99.7%, Sigma-Aldrich) with slightly excess of 1-bromodecane (0.44 mol, 98%, Sigma-Aldrich). The flask was equipped with a stir bar and refluxed at 110 °C using an oil bath for 24 h. Toluene was carefully removed by rotavapor then the product was further washed with diethyl ether (200 mL, ≥99.5%, Sigma-Aldrich) for 3 times. [C₁₀MIM]Br was obtained as yellowish viscous oil (yield: 88%).

For the metathesis reaction, [C₁₀MIM]Br was firstly dissolved in absolute ethanol (≥99.8%, Fisher Scientific) with KOAc (≥99%, Sigma-Aldrich), then above mixture was stirred at ambient temperature for at least 2 h. Slight excess of KOAc was necessary to guarantee the displacement of Br⁻. A White precipitate was filtered to separate the insoluble KBr out of solution, where the latter was evaporated by rotavapor to remove ethanol. Cold acetone (≥99.8%, Fisher Scientific) was then added and the flask was left in refrigerator for 12 h to totally precipitate KBr and excessive KOAc. After filtering again, potassium salts were totally removed, the remaining acetone was removed by rotavapor. The product was further purified under high vacuum at 50 °C overnight. [C₁₀MIM][OAc] was finally obtained as yellowish oil, less viscous than [C₁₀MIM]Br (yield: 94%).

2) Characterisation

Nuclear magnetic resonance (NMR) spectroscopy. The synthesised ILs were characterised by 1D NMR spectroscopy to ensure no detectable impurity with chloroform-d as solvent. Proton spectra were recorded on Bruker Avance III 400 MHz NMR spectrometer. 2D ^{1}H-^{1}H NOESY is a very sensitive spectroscopic technique to examine the spatial microenviroment of protons by measuring spin-lattice relaxation. All IL/water/phenolic compound ternary mixtures were studied by 2D NMR experiments where dimethyl sulfoxide-d6 (DMSO-d6) was used as external standard. NEOSY spectra were recorded on Bruker 600 MHz NMR spectrometer.

1-decyl-3-methylimidazolium bromide

^{1}H NMR (chloroform-d, 400 MHz): δ 10.11 (s, 1 H), 7.58 (s, 1 H), 7.38 (s, 1 H), 4.15 (t, 2 H), 3.96 (s, 3 H), 1.73 (m, 2 H), 1.00-1.20 (m, 14 H), 0.68 (t, 3 H). ^{13}C NMR (chloroform-d, 100 MHz): δ 137.0, 123.8, 122.1, 50.0, 36.6, 31.7, 30.2, 29.3, 29.2, 29.1, 28.8, 26.1, 22.5, 13.9.

1-decyl-3-methylimidazolium acetate

^{1}H NMR (chloroform-d, 400 MHz): δ 10.80 (s, 1 H), 7.39 (s, 1 H), 7.35 (s, 1 H), 4.06 (t, 2 H), 3.87 (s, 3 H), 1.72 (m, 2 H), 1.72 (m, 3 H), 0.80-1.30 (m, 14 H), 0.64 (t, 3 H). ^{13}C NMR (chloroform-d, 100 MHz): δ 177.1, 139.2, 123.2, 121.5, 49.6, 35.9, 31.5, 30.1, 29.1, 29.0, 28.9, 28.7, 26.0, 25.4, 22.4, 13.9.

Small-angle X-ray Scattering (SAXS). SAXS experiments were recorded by the Offline DL-SAXS instrument Xeuss 3.0 (Excillium Ga MetalJet source, 9.2 keV, λ=0.71 Å) in Diamond Light Source, Harwell Campus, Oxfordshire. The sample was transferred into a capillary (1.5 mm of outer diameter) and sealed tightly. Measurements were carried out under vacuum at variable temperatures with a detector to sample distance of 275 mm to ensure all possible characteristic

peaks detected (q range 0.05-1.13 Å^{-1}). An acquisition time of 300 s was used for all the samples. Data was corrected by subtraction of transmission and background scattering. The intensity was plotted versus scattering vector, *q=(4πsinθ)/λ*.

Polarised optical microscopy (POM). Phase examinations were performed under an Olympus BX50 microscope. All samples' textures were determined at 298.15 K with a Linkam TH600 hot stage and TP 92 temperature controller.

Supplementary results

Figure S2 shows the POM images for mixtures without and with phenol added, respectively. At the same water content of 18 wt%, IL/water binary mixture exhibited a lyotropic liquid crystalline structure. Combined with Figure S3, it can be deduced that this liquid crystalline phase is dominatingly composed of hexagonal columnar micelles. When equimolar of phenol with ILs are added into the mixture, the crystalline phase disappeared leaving a clear liquid phase.
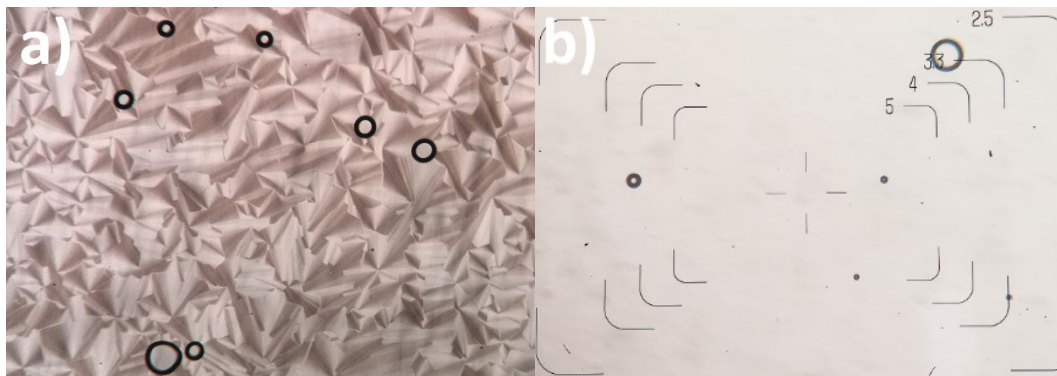

Figure S2 POM images at 18 wt% of water: a) [C$_{10}$MIM][OAc]/water binary mixture; b) [C$_{10}$MIM][OAc]/water/phenol ternary mixture

Figure S3a shows the SAXS profiles of IL/water binary mixtures with varying water contents. The characteristic scattering vector ratio $q_1:q_2:q_3$ = 1:$\sqrt{3}$:$\sqrt{4}$ in mixture containing 18-50 wt% of water confirmed the dominating hexagonal columnar phase. With the increasing of water content, the mixture gradually lost its crystalline structure. Figure S3b shows the final configuration of IL/water binary mixture with 18.2 wt% of water; an evident hexagonal array can be observed. The hydrophobic alkyl chain (cyan beads) of IL cation aggregates to form the core of micelles, while imidazolium ring (red beads) and acetate anion (blue beads) reside in hydrophilic phase where water (white beads) resides.

This results for IL/water binary mixtures show similar trend with the reports for other anions based ILs. With the same cation, the liquid crystalline phase for [C_{10}MIM][Br] ionogels, as well as nitrate-based ionogels, undergoes: lamellar, hexagonal perforated layers and hexagonal phases when the weighted concentration of water in the system ranges from 11-16%, 17% and 40% respectively.[35] Goodchild et al[36] studied the phase behaviour of [C_{10}MIM][Cl]/water mixture through ^{1}H NMR technique. Hexagonal columnar morphology was found to be the major mesophase at the water concentrations from 6-44% by weight.

Figure S3c depicts the influence of temperature on SAXS profiles for [C_{10}MIM][OAc]/water binary mixture. At a fixed water content of 34 wt%, there is a diminishing effect on the characteristic scattering peaks with the growing temperature. Eventually, only a single broad scattering peak remains at 358.15 K. This can be attributed that higher temperature brings increased kinetic energy, so the fixed liquid crystalline lattice was disrupted, leaving a dynamic short-range structural ordering.
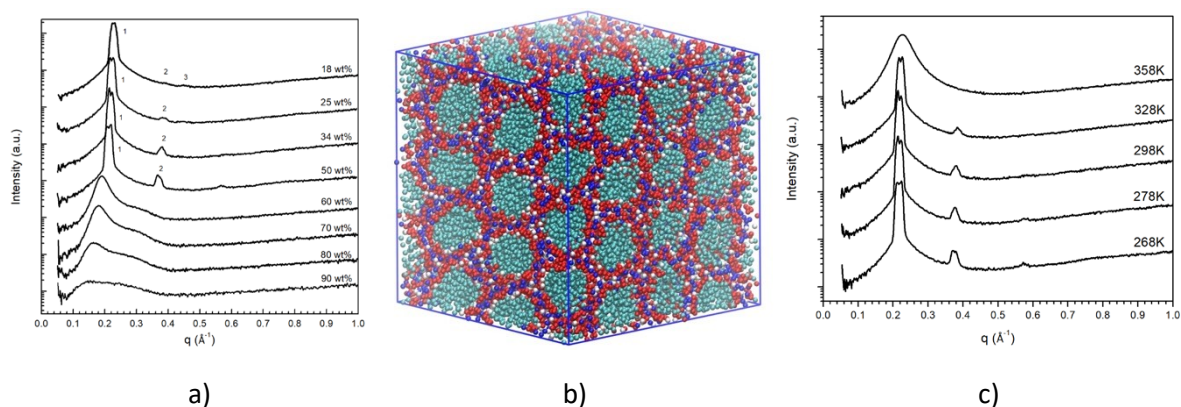

a)   b)   c)

Figure S3 a) SAXS spectra of [C_{10}MIM][OAc]/water binary mixtures with varying water contents at 25 °C; b) snapshot from MD simulation of [C_{10}MIM][OAc]/water binary mixtures with 18.2 wt% of water; and c) SAXS spectra of [C_{10}MIM][OAc]/water binary mixture containing 34 wt% of water at various temperatures

Figure S4 shows the SAXS profiles of IL/water/phenol ternary mixtures with three different water contents at 263.15 K. Lower temperature brings lower kinetic energy and slower molecule motions. More recognisable scattering peaks were detected. At 18 wt%, the scattering vector ratio $q_1:q_2=1:2$ indicates that the mixture has dominating smectic lamellar bilayer structures. At 44 wt%, the scattering vector ratio $q_1:q_2=1:\sqrt{3}$ indicates the presence of hexagonal columnar arrays. At higher water content of 90 wt%, the two peaks merged into a much broader peak, which means the mixture likely lost its ordering and spherical clusters with different diameters were formed.
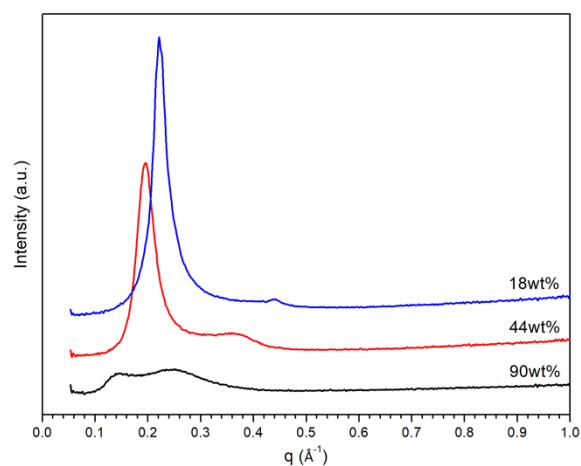

Figure S4 SAXS patterns of [C_{10}MIM][OAc]/phenol/water ternary mixtures at 263.15 K

The SAXS profiles of ternary mixtures at varying temperatures are shown in Figure S5. All scattering peaks become higher with the decreasing temperature. As shown in Figure S5a and b, ternary mixture containing phenol at lower temperatures showed more recognisable scattering peaks, especially at 263 K. At 34 wt% of water, the scattering ratio of $q_1:q_2=1:\sqrt{3}$ indicates the dominating hexagonal columnar phase. At 18 wt% of water, the scattering ratio of $q_1:q_2=1:2$ confirms the formation of lamellar bilayer structures. However, for ternary mixtures containing resorcinol or phloroglucinol, lower temperature does not manifest other scattering peaks such as q_2 peak in their phenol counterpart.
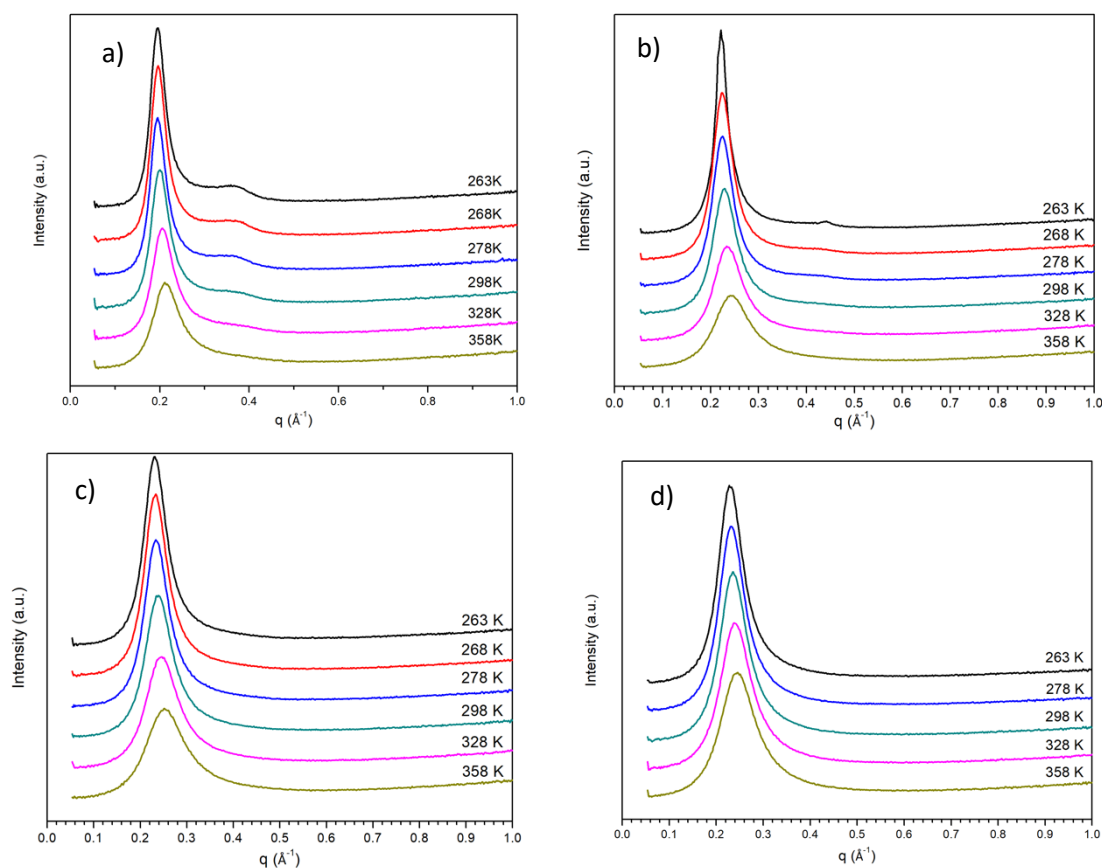

Figure S5 SAXS profiles for ternary mixtures at various temperatures for different precursors: a) phenol at 34 wt% of water, b) phenol at 18wt% of water, c) resorcinol at 18wt% of water, and d) phloroglucinol at 18wt% of water.

Figure S6a shows the representative POM image of ternary mixture containing benzene, where the small cross pattern can be attributed to the formation of lamellar bilayer liquid crystalline structures. When the precursors are added quantitatively less than [C$_{10}$MIM][OAc], two phases are observed for ternary mixtures containing resorcinol or phloroglucinol: isotropic liquid phase and lyotropic liquid crystals.
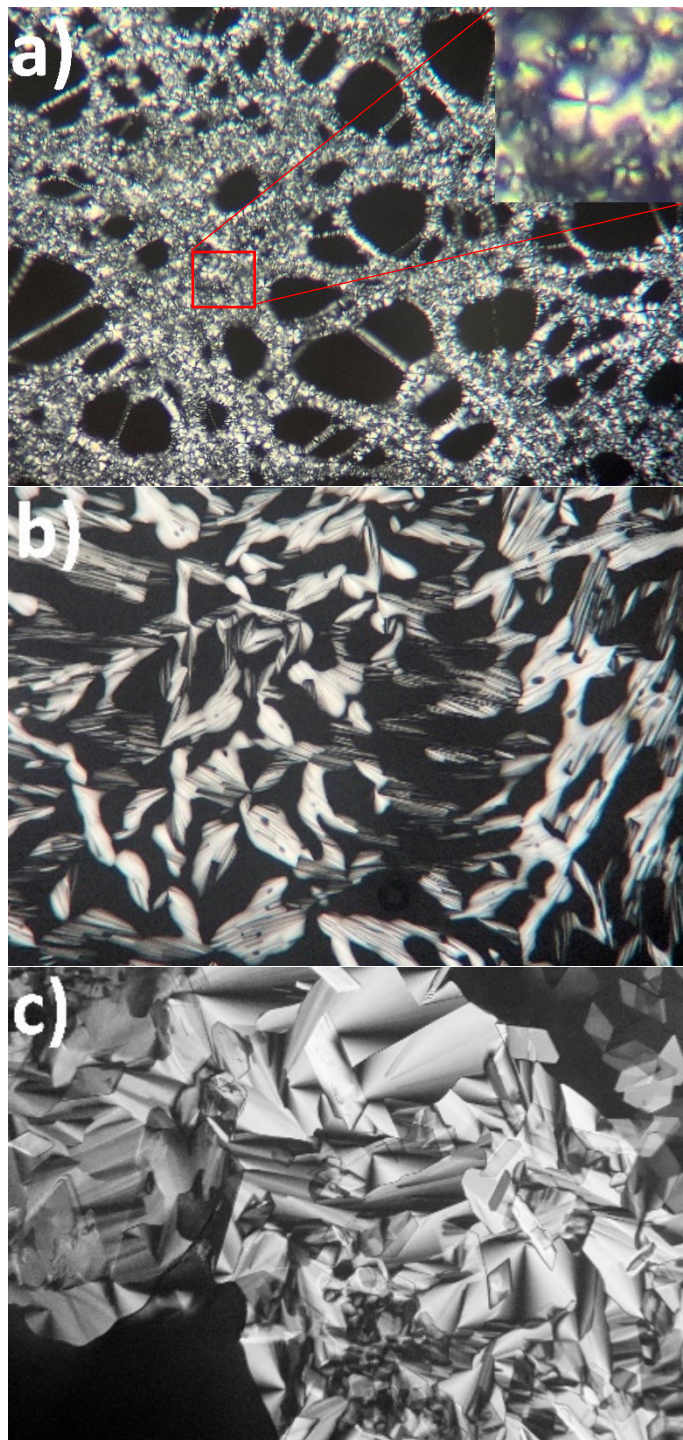

Figure S6 Representative POM images of lyotropic phase for ternary mixtures at around 18 wt% of water: a) ternary mixture containing benzene at [C$_{10}$MIM][OAc]/benzene ratio of 1:1; b) [C$_{10}$MIM][OAc]/water/resorcinol at [C$_{10}$MIM][OAc]/precursor ratio of 1:0.5; c) [C$_{10}$MIM][OAc]/water/phloroglucinol at [C$_{10}$MIM][OAc]/precursor ratio of 1:0.5

Table S2 summarises all the H-bonding interaction energies obtained by NBO analysis for ternary systems containing phloroglucinol, resorcinol, phenol, and benzene, respectively. The parameters found by the NBO and QTAIM analysis for each single significant H-bond found for the different phenolic systems are shown in Table S3, with the percentage of the total interaction energy these H-bonds contribute shown in Figure S7. In general, the different parameters found by QTAIM and NBO analysis were in good agreement as to the relative strength of the H-bonds. The strengths of H-bonds were approximately the same for the different phenolic compounds, with the main difference being an increase in the number of significant H-bonds and an increase in the percentage of the total interaction contributed by H-bonds for the phenolics with more hydroxyl groups. Indeed, only three significant H-bonds were found for the benzene system whereas nine significant H-bonds were found for the phloroglucinol system. Three water-H…acetate bonds were found for every system, with a single phenolic-H…acetate involving the hydrogen of the hydroxyl group, except for benzene as without the presence of the hydroxyl group was not able to form this type of H-bond. Above these four H-bonds, the acetate/anion displays a saturation(-like) effect and did not form any further significant H-bonds. According to most of the metrics given in Table S3, these H-bonds where acetate is the hydrogen acceptor were the strongest formed, with acetate-H…water strongest for the benzene and resorcinol systems and acetate-H…phenolic strongest for the phenol and resorcinol. The resorcinol and phloroglucinol systems also display a strong H-bond of type phenolic-H…water, with the phloroglucinol system also displaying a weaker bond of type water-H…phenolic. Interestingly, the contribution of addition significant H-bonds with increasing hydroxyl groups can only partially be explained by bonds where the phenolic is directly involved. Indeed, the resorcinol and phloroglucinol also display a significant water-cation H-bond and an increase in the number of significant water-water H-bonds can also be seen from only one for phenol to two for resorcinol and phloroglucinol. This indicates that the different phenolic compounds influence the ability of other molecules in the system to form H-bonds, although these addition not directly phenolic bonds are weaker than the phenolic or acetate H-bonds. The lack of a dramatic increase in the number of H-bonds directly involving the hydroxyl group of resorcinol and phloroglucinol can be observed. This could be further evidence that the smaller system size of the DFT calculations may have an effect, namely in causing some of the possible H-bonds of the hydroxyl group being neglected due to the lack of neighbouring ionic liquid systems, causing the differences in H-bonding between phenol and resorcinol/phloroglucinol as calculated by DFT to be smaller than in reality. For instance, only one oxygen of a phenolic is a H-acceptor for only the phloroglucinol situation displaying that this type of bonding is possible yet does not occur frequently in the DFT modelling due to the additional hydroxyl groups of the resorcinol and phloroglucinol molecules being in a position where they do not form bonds with molecules from neighbouring ionic liquid systems which would be there in reality. This could be attributed to the low water content in mixtures, around 18 wt% and there is strong competition to form H-bonds between [C$_{10}$MIM][OAc], water, and phenolic compounds.

Table S2. H-bonding interaction energy within ternary systems.

Hydrogen bonds	Ternary mixtures			
	phloroglucinol	resorcinol	phenol	benzene
acetate … H-cation	4.85	6.02	0.88	25.31
acetate … H-water	174.72	220.62	202.00	244.35
acetate … H-phenolic	134.14	74.48	133.93	0.00
water … H-cation	46.74	37.24	39.16	13.64
water … H-acetate	0.00	0.00	2.93	0.00
water … H-water	72.22	55.90	39.54	39.71
water … H-phenolic	88.28	84.52	0.00	6.23
phenolic … H-cation	0.00	0.00	0.84	0.00
phenolic … H-acetate	0.00	0.00	1.30	0.00
phenolic … H-water	18.58	2.76	9.62	0.00
Total energy (kJ/mol)	539.53	481.54	430.20	329.24

Table S3 Parameters found by QTAIM and NBO analysis for each significant H-bond in ternary mixtures

benzene

molecules involved	bond length (A)	ρ_{BCP} (a.u.)	$\nabla^2\rho_{BCP}$ (a.u.)	H_{BCP}	H-bond energy from ρ_{BCP} (kJ/mol)	E2 kJ/mol
water-H...acetate	1.677	0.04752	0.12699	-0.00904	-70.54	124.60
water-H...acetate	1.767	0.03892	0.12009	-0.00401	-58.57	84.10
water-H...acetate	1.929	0.02443	0.10520	0.00239	-38.43	22.22

phenol

molecules involved	bond length (A)	ρ_{BCP} (a.u.)	$\nabla^2\rho_{BCP}$ (a.u.)	H_{BCP}	H-bond energy from ρ_{BCP} (kJ/mol)	E2 kJ/mol
phenolic-H...acetate	1.642	0.04954	0.1362	-0.00980	-73.35	128.74
water-H...acetate	1.714	0.04317	0.1254	-0.00648	-64.49	88.32
water-H...acetate	1.796	0.03322	0.1200	-0.00087	-50.66	55.77
water-H...acetate	1.803	0.03429	0.1178	-0.00162	-52.14	57.91
water-H...water	1.909	0.02690	0.1003	0.00095	-41.87	40.04

resorcinol

molecules involved	bond length (A)	ρ_{BCP} (a.u.)	$\nabla^2\rho_{BCP}$ (a.u.)	H_{BCP}	H-bond energy from ρ_{BCP} (kJ/mol)	E2 kJ/mol
phenolic-H...acetate	1.795	0.03490	0.1152	-0.00221	-52.99	74.48
water-H...acetate	1.634	0.04992	0.1378	-0.00994	-73.88	113.47
water-H...acetate	1.798	0.03318	0.1162	-0.00121	-50.59	57.82
water-H...acetate	1.861	0.03077	0.1084	-0.00033	-47.24	49.33
cation-H...water	2.072	0.02036	0.0774	0.00251	-32.78	33.60
phenolic-H...water	1.761	0.03852	0.1182	-0.00413	-58.03	84.52
water-H...water	1.967	0.02375	0.0912	0.00176	-37.49	30.92
water-H...water	1.988	0.02285	0.0913	0.00211	-36.23	24.98

phloroglucinol

| molecules involved	bond length (A)	ρ_{BCP} (a.u.)	$\nabla^2\rho_{BCP}$ (a.u.)	H_{BCP}	H-bond energy from ρ_{BCP} (kJ/mol)	E2 kJ/mol
phenolic-H...acetate	1.650	0.04845	0.1360	-0.00911	-71.83	131.46
water-H...acetate	1.691	0.04047	0.1421	-0.00364	-60.74	84.18
water-H...acetate	1.811	0.03394	0.1139	-0.00175	-51.65	56.36
water-H...acetate	1.920	0.02567	0.1005	0.00152	-40.15	30.84
cation-H...water	1.999	0.02420	0.0902	0.00196	-38.12	45.02
phenolic-H...water	1.736	0.03987	0.1236	-0.00451	-59.90	88.28
water-H...phenolic	1.977	0.02125	0.0895	0.00267	-34.01	18.58
water-H...water	1.929	0.02687	0.0979	0.00083	-41.83	38.66
water-H...water	1.942	0.02542	0.0977	0.00148	-39.81	32.05
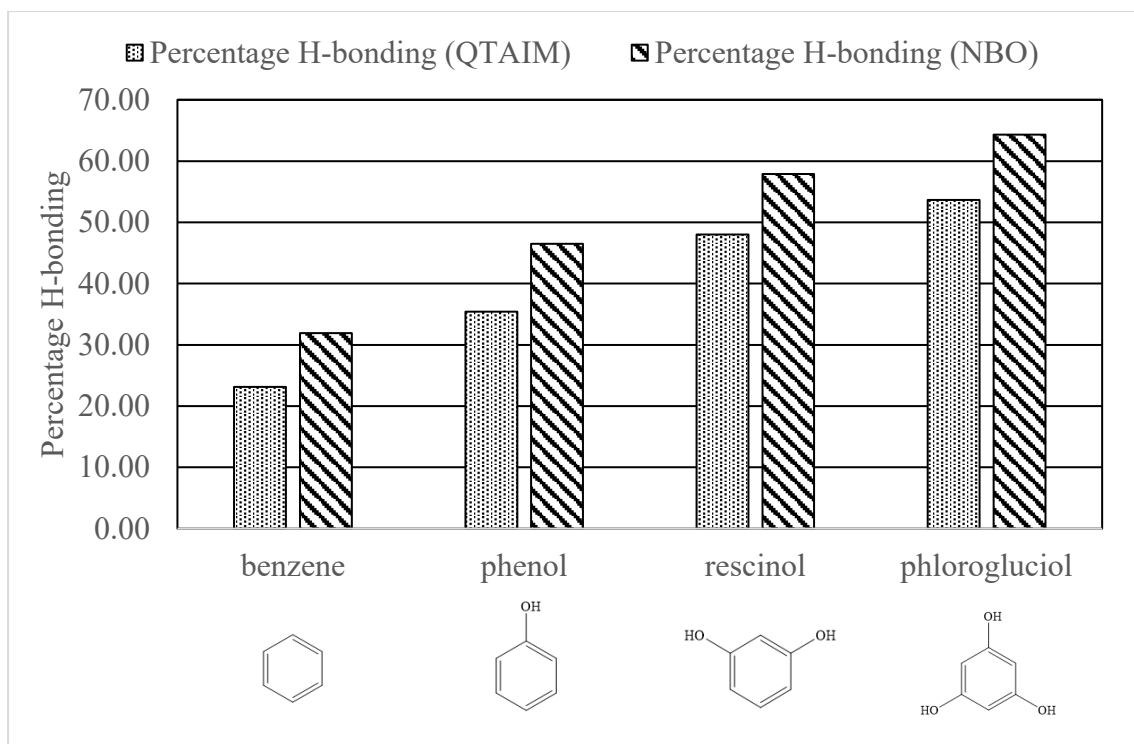
Figure S7 Percentage of H-bonding contribution to total interaction energy as measured by QTAIM and NBO analysis methods.
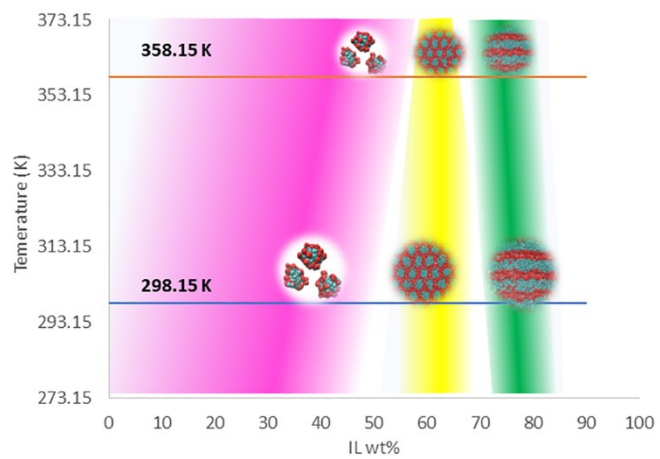
Figure S8 Influence of temperature on the morphology evolution of [C$_{10}$MIM][OAc]/water/phenol ternary mixtures
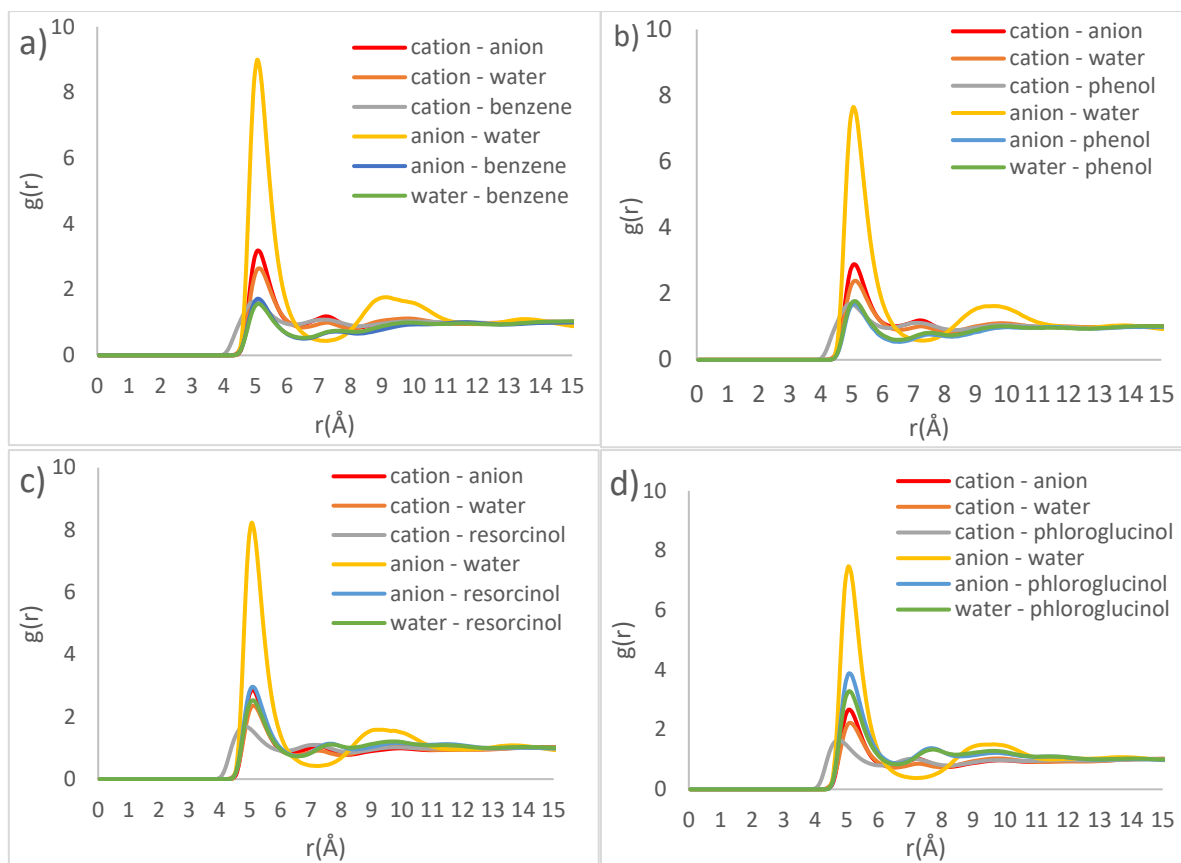
Figure S9 COM RDFs for ternary systems containing a) benzene, b) phenol, c) resorcinol, and d) phloroglucinol, respectively.

From Table S3 and Figure 8, a clear trend is found that precursors with the increasing hydroxyl group were dispersed further from the terminal carbon of alkyl chain. The closer proximity of the phenolic compound and the Imidazolidine ring appears to have the effect of straightening out the cation causing the angle between the chain and the Imidazolidine ring to approach 180°. This has the additional consequence of causing a closer to parallel orientation between the phenolic and Imidazolidine ring structures, which will likely induce dispersive interactions between the rings. The phenolic compound resides closer to the cation, which would be expected with the stronger interaction between the two molecules. A potential explanation of this is that the additional hydroxyl groups causing a stronger phenolic-ionic interaction allowing the phenolic compounds to disrupt the interactions, allowing the phenolic compounds to occupy the space between the anion and cation. This would also explain the weaker ionic-ionic and water-ionic found with more hydroxyl groups present.

Table S4 Molecular geometry parameters for each phenolic compound in relation to the cation

Ternary mixtures containing various precursors	d1 (Å) (end chain to centre of phenolic compound ring)	d2 (Å) (nearest chain carbon to centre of phenolic compound ring)
benzene	6.15	3.52
phenol	8.36	3.51
resorcinol	10.91	3.39
phloroglucinol	15.55	3.13

References

1   K. Goloviznina, J. N. Canongia Lopes, M. Costa Gomes and A. A. H. Pádua, *J. Chem. Theory Comput.*, 2019, **15**, 5858–5871.

2   B. Doherty, X. Zhong and O. Acevedo, *J. Phys. Chem. B*, 2018, **122**, 2962–2974.

3   J. N. Canongia Lopes and A. A. H. Pádua, *Theor. Chem. Acc.*, 2012, 131, 1–11.

4   B. L. Bhargava, R. Devane, M. L. Klein and S. Balasubramanian, *Soft Matter*, 2007, **3**, 1395–1400.

5   B. L. Bhargava and M. L. Klein, *Mol. Phys.*, 2009, **107**, 393–401.

6   Y. Wang, S. Feng and G. A. Voth, *J. Chem. Theory Comput.*, 2009, **5**, 1091–1098.

7   Y. Wang, S. Izvekov, T. Yan and G. A. Voth, *J. Phys. Chem. B*, 2006, **110**, 3564–3575.

8   Y. Wang, W. Jiang, T. Yan and G. A. Voth, *Acc. Chem. Res.*, 2007, **40**, 1193–1199.

9   Y. Wang and G. A. Voth, *J. Am. Chem. Soc.*, 2005, **127**, 12192–12193.

10   D. Roy and M. Maroncelli, *J. Phys. Chem. B*, 2010, **114**, 12629–12631.

11   D. Roy, N. Patel, S. Conte and M. Maroncelli, *J. Phys. Chem. B*, 2010, **114**, 8410–8424.

12   C. Merlet, M. Salanne, B. Rotenberg and P. A. Madden, *J. Phys. Chem. C*, 2011, **115**, 16613–16618.

13   C. Merlet, M. Salanne and B. Rotenberg, *J. Phys. Chem. C*, 2012, **116**, 7687–7693.

14   D. Sun and J. Zhou, *AIChE J.*, 2013, **59**, 2630–2639.

15   A. Moradzadeh, M. H. Motevaselian, S. Y. Mashayak and N. R. Aluru, *J. Chem. Theory Comput.*, 2018, **14**, 3252–3261.

16   H. A. Karimi-Varzaneh, F. Müller-Plathe, S. Balasubramanian and P. Carbone, *Phys. Chem. Chem. Phys.*, 2010, **12**, 4714–4724.

17   E. A. Crespo, N. Schaeffer, J. A. P. Coutinho and G. Perez-Sanchez, *J. Colloid Interface Sci.*, 2020, **574**, 324–336.

18   Y. L. Wang, B. Li, S. Sarman, F. Mocci, Z. Y. Lu, J. Yuan, A. Laaksonen and M. D. Fayer, *Chem. Rev.*, 2020, 120, 5798–5877.

19   D. Bedrov, J. P. Piquemal, O. Borodin, A. D. Mackerell, B. Roux and C. Schröder, *Chem. Rev.*, 2019, 7940–7995.

20   B. L. Bhargava, Y. Yasaka and M. L. Klein, *Chem. Commun.*, 2011, **47**, 6228–6241.

21   M. Salanne, *Phys. Chem. Chem. Phys.*, 2015, **17**, 14270–14279.

22   S. J. Marrink, H. J. Risselada, S. Yefimov, D. P. Tieleman and A. H. De Vries, *J. Phys. Chem. B*, 2007, **111**, 7812–7824.

23   G. Huet, M. Araya-Farias, R. Alayoubi, S. Laclef, B. Bouvier, I. Gosselin, C. Cézard, R. Roulard, M. Courty, C. Hadad, E. Husson, C. Sarazin and A. Nguyen Van Nhien, *Green Chem.*, 2020, **22**, 2935–2946.

24   D. H. De Jong, G. Singh, W. F. D. Bennett, C. Arnarez, T. A. Wassenaar, L. V. Schäfer, X. Periole, D. P. Tieleman and S. J. Marrink, *J. Chem. Theory Comput.*, 2013, **9**, 687–697.

25   R. Alessandri, J. J. Uusitalo, A. H. De Vries, R. W. A. Havenith and S. J. Marrink, *J. Am. Chem. Soc.*, 2017, **139**, 3697–3705.

26   L. Martinez, R. Andrade, E. G. Birgin and J. M. Martínez, *J. Comput. Chem.*, 2009, **30**, 2157–2164.

27   G. J. Martyna, D. J. Tobias and M. L. Klein, *J. Chem. Phys.*, 1994, **101**, 4177–4189.

28   S. Nose, *Mol. Phys.*, 2002, **100**, 191–198.

29   W. G. Hoover, *Canonical dynamics: Equilibrium phase-space distributions*, 1985, vol. 31.

30   S. Plimpton, *J. Comput. Phys.*, 1995, **117**, 1–19.

31   W. Humphrey, A. Dalke and K. Schulten, *J. Mol. Graph.*, 1996, **14**, 33–38.

32   D. J. Frisch, M. J.; Trucks, G. W.; Schlegel, H. B.; Scuseria, G. E.; Robb, M. A.; Cheeseman, J. R.; Scalmani, G.; Barone, V.; Petersson, G. A.; Nakatsuji, H.; Li, X.; Caricato, M.; Marenich, A. V.; Bloino, J.; Janesko, B. G.; Gomperts, R.; Mennucci, B.; Hratch, *Gaussian Inc., Wallingford CT*, 2016.

33   T. Lu and F. Chen, *J. Comput. Chem.*, 2012, **33**, 580–592.

34   S. Emamian, T. Lu, H. Kruse and H. Emamian, *J. Comput. Chem.*, 2019, **40**, 2868–2881.

35   M. A. Firestone, P. G. Rickert, S. Seifert and M. L. Dietz, *Inorganica Chim. Acta*, 2004, **357**, 3991–3998.

36   I. Goodchild, L. Collier, S. L. Millar, I. Prokeš, J. C. D. Lord, C. P. Butts, J. Bowers, J. R. P. Webster and R. K. Heenan, *J. Colloid Interface Sci.*, 2007, **307**, 455–468.